MICROROBOTS

Light-driven carbon nitride microswimmers with propulsion in biological and ionic media and responsive on-demand drug delivery

Varun Sridhar[1], Filip Podjaski[2]*, Yunus Alapan[1], Julia Kröger[2,3], Lars Grunenberg[2,3], Vimal Kishore[1,4], Bettina V. Lotsch[2,3,5]*, Metin Sitti[1,6,7]*

We propose two-dimensional poly(heptazine imide) (PHI) carbon nitride microparticles as light-driven microswimmers in various ionic and biological media. Their high-speed (15 to 23 micrometer per second; 9.5 ± 5.4 body lengths per second) swimming in multicomponent ionic solutions with concentrations up to 5 M and without dedicated fuels is demonstrated, overcoming one of the bottlenecks of previous light-driven microswimmers. Such high ion tolerance is attributed to a favorable interplay between the particle's textural and structural nanoporosity and optoionic properties, facilitating ionic interactions in solutions with high salinity. Biocompatibility of these microswimmers is validated by cell viability tests with three different cell lines and primary cells. The nanopores of the swimmers are loaded with a model cancer drug, doxorubicin (DOX), resulting in a high (185%) loading efficiency without passive release. Controlled drug release is reported under different pH conditions and can be triggered on-demand by illumination. Light-triggered, boosted release of DOX and its active degradation products are demonstrated under oxygen-poor conditions using the intrinsic, environmentally sensitive and light-induced charge storage properties of PHI, which could enable future theranostic applications in oxygen-deprived tumor regions. These organic PHI microswimmers simultaneously address the current light-driven microswimmer challenges of high ion tolerance, fuel-free high-speed propulsion in biological media, biocompatibility, and controlled on-demand cargo release toward their biomedical, environmental, and other potential applications.

INTRODUCTION

Microswimmers are cell-scale mobile machines that can be self-propelled by converting energy made available to them from their environment or remotely (*1*–*3*), such as chemical reagents, light, and magnetic or acoustic energy (*4*, *5*). One of the main targeted applications of microswimmers is local, active, and on-demand delivery of theranostic cargos, such as drugs, imaging agents, and stem cells inside the human body and organ-on-a-chip devices (*6*–*8*). So far, chemical propulsion—for example, by dissolution of metals (e.g., magnesium under acidic conditions)—enzymatic, and magnetic propulsion are the most widely used methods in such in vitro and in vivo biomedical applications (*9*). Chemical propulsion is predominantly used for swimming in acidic body fluids, such as inside the stomach and gastrointestinal tract (*9*–*12*), whereas enzymatic propulsion can be used in other body regions (*13*–*15*). Both methods need sacrificial and usually toxic agents as fuels to enable swimming, which is disadvantageous for their prolonged use under biological conditions (*16*). Light, however, is a viable energy source for the propulsion of microswimmers (*17*, *18*), both with and without the use of additional fuels, enabling also propulsion control and steering (*19*, *20*). Moreover, photocatalytic swimmers can exhibit positive and negative phototaxis and gravitaxis (*21*), depending on their surface charge (*22*), enabling their steering control and targeting a desired location (*23*).

Despite their many advantages over other self-propulsion methods, photocatalytic and chemical propulsion suffer from fundamental propulsion limitations in electrolyte solutions (*18*), especially when diffusiophoretic and electrophoretic propulsion modes are operative. This drawback is due to the presence of ions hindering the build-up of concentration gradients of reactants and products involved in self-electrophoresis and self-diffusiophoresis around the swimmer (*24*–*26*). Although different semiconducting inorganic photocatalysts (*27*–*32*) have been studied as light-driven microswimmers for potential biological applications (*33*), donor-free light-driven swimming in ionic media has only been demonstrated with sophisticated geometries in Si for concentrations below 10 mM. Thus, light-driven swimming in ionic media—such as NaCl, Dulbecco's phosphate-buffered saline (dPBS), and Dulbecco's modified Eagle's medium (DMEM)—with concentration levels of more than 200 mM present in various biological solutions and cell environments still remains an unresolved bottleneck. The EI50 number has been introduced previously as a measure of the ionic concentration at which the speed of the microswimmers is reduced by 50% (*34*). EI50 is less than 0.1 mM for self-diffusiophoretic and self-electrophoretic swimmers (*25*), reaching up to ~4 mM for geometrically optimized systems addressing this problem (*34*).

For biomedial applications, an EI50 value of more than 100 mM is required. This limitation is attributed to the presence of a solid surface in the microswimmer, which does not allow fluids or ions to migrate through the swimmer. The presence of salt ions reduces the Debye length of the electrochemical layer formed on the surface of the microswimmers in contact with the solution from hundreds of

[1]Physical Intelligence Department, Max Planck Institute for Intelligent Systems, 70569 Stuttgart, Germany. [2]Nanochemistry Department, Max Planck Institute for Solid State Research, 70569 Stuttgart, Germany. [3]Department of Chemistry, Ludwig-Maximilians-Universität München, 81377 Munich, Germany. [4]Department of Physics, Banaras Hindu University, Varanasi 221005, India. [5]Cluster of Excellence e-conversion, Lichtenbergstrasse 4, 85748 Garching, Germany. [6]Institute for Biomedical Engineering, ETH Zurich, 8092 Zurich, Switzerland. [7]School of Medicine and College of Engineering, Koç University, 34450 Istanbul, Turkey.
*Corresponding author. Email: sitti@is.mpg.de (M.S.); b.lotsch@fkf.mpg.de (B.V.L.); f.podjaski@fkf.mpg.de (F.P.)

nanometers to ~1 nm (*35*), thereby collapsing also the ionic gradient around the particle under illumination, which is responsible for the propulsion force. Therefore, commonly, the collapse of the Debye layer stops the swimming for hard spheres. Besides, most light-driven microswimmers require high concentrations of H_2O_2 or alcohols as additional chemical fuels (*36*), which should be avoided in biological applications because of their toxicity. The availability of potential biocompatible fuels that are present in large enough quantities has been a pressing bottleneck in implementing light-driven microswimmers in such applications (*18*), which require concentrations as high as ~30 mM of biocompatible fuels like glucose for effective light-driven propulsion (*37*). Furthermore, taxis-based direction-controlled propulsion and controlled cargo uptake and release of active products are highly desired properties of medical microswimmers, which are usually studied and realized separately (*38*).

Here, we aim to solve the above issues and bottlenecks by using highly (photocatalytically) active and porous (texturally and structurally) carbon nitrides (CN_x) as light-driven microswimmers. CN_x are a family of organic macromolecular photocatalysts that have gained attention because of their facile synthesis (*39*), chemical robustness, absorption of visible light, and favorable band positions that enable various photocatalytic redox reactions, such as water splitting (*40*). Besides, CN_x are widely used for environmental remediation (*41*), sensing, and ion pumping (*41–43*). Most commonly, a one-dimensional (1D) CN_x called "melon" or "g-C_3N_4" is reported. However, in this study, we use a recently found 2D CN_x species called poly(heptazine imide) (PHI) (*44–46*), which hosts hydrated alkali metal ions (typically K^+) or protons in its structural nanopores, resulting in an unusual blend of optoelectronic and optoionic properties (*47–49*). PHI does not only show higher hydrogen evolution activity than melon-type CN_x (*44*, *45*, *50*), but it is also able to store light-induced electrons for subsequent use through electron-ion interactions (*47–49*, *51*). Because PHI microswimmers exhibit not only structural but also textural porosity, enabling ion intercalation and permeability that can be driven by light (*42*, *46–48*), they are promising platforms for light-driven propulsion (*51*) and cargo delivery in various biological media, while not requiring sophisticated shape control. Hence, the development of biocompatible and highly ion-tolerant, nontoxic light-driven microswimmers that can be propelled purely by visible light in naturally occurring biofuels while being able to carry and release cargo in a controllable fashion may solve many fundamental challenges (*48*).

RESULTS

PHI characterization

The PHI microparticles were obtained by sonication and centrifuge-assisted separation from the original suspension (see Materials and Methods for details). Figure 1A shows a scanning electron microscopy (SEM) image of the PHI microparticles with a diameter ranging from 1 to 5 μm. Because they represent agglomerates of smaller primary crystallites, the microswimmers have an irregular spherical shape, and textural nanopores occur spontaneously. These larger voids enable efficient fluid movement and entrapment. Figure 1 (B) illustrates the underlying molecular structure of the PHI microswimmers. Structural nanopores in the PHI backbone consisting of imide-bridged heptazine units are filled with hydrated

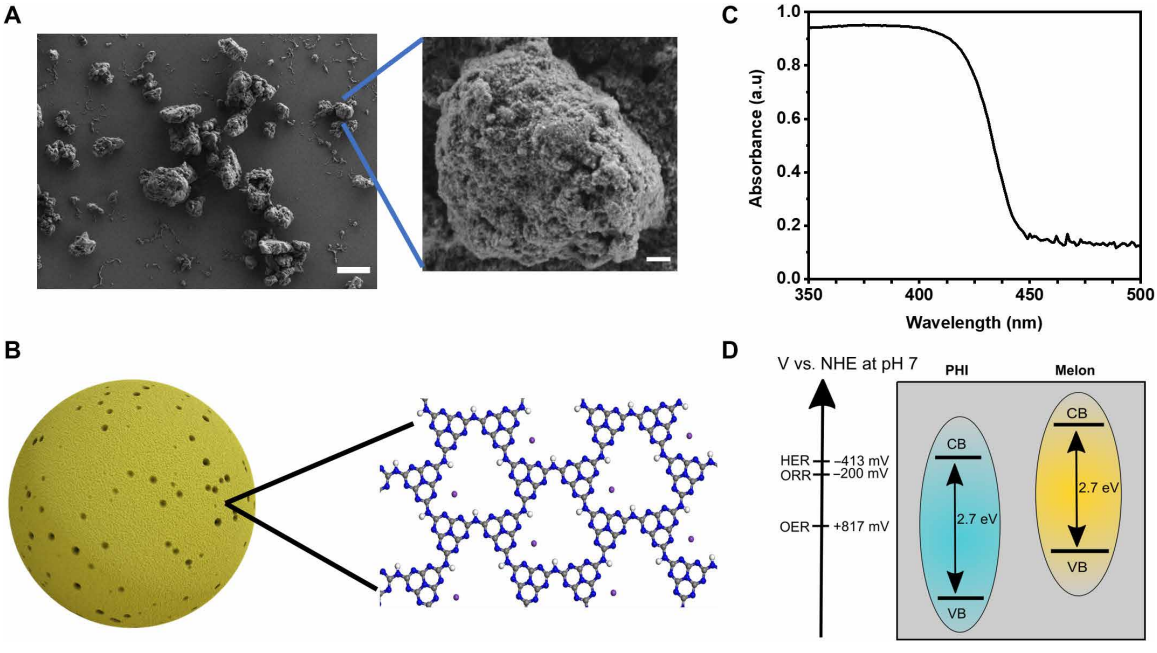

Fig. 1. Structure, morphology, and optical properties of PHI-based organic microswimmer particles. (**A**) SEM image of representative PHI microparticles (gray) with a size distribution of 1 to 5 μm (scale bar, 5 μm) and close-up of one particle (scale bar, 400 nm), showing the porous morphology. (**B**) Schematics of the PHI microswimmer and structure of the PHI macromolecules consisting of heptazine moieties comprising carbon (blue), nitrogen (gray), and hydrogen (white). Solvated potassium ions reside in structural nanopores (purple). (**C**) Absorbance spectrum of PHI microswimmers, showing the onset of bandgap absorption at 450 nm determined on the basis of a Tauc plot. a.u, arbitrary unit. (**D**) Band positions of PHI and melon with a bandgap of 2.7 eV along with hydrogen evolution reaction (HER), oxygen reduction reaction (ORR), and oxygen evolution reaction (OER) potentials at pH of 7.

ions that can be exchanged (*46*). The absorbance spectrum in Fig. 1C shows light absorption below 450 nm (bandgap of 2.7 eV) (*47*, *49*), enabling photocatalysis and, hence, propulsion driven by visible light. The strongly positive valence band position (+2.2 V versus normal hydrogen electrode) gives rise to an even stronger oxidative power of the light-generated holes than for melon (Fig. 1D) (*47*), providing the thermodynamic driving force for various photocatalytic oxidation reactions, including water oxidation, which are often the bottleneck for light-generated charge extraction and photocatalytic propulsion (*51*).

Light-induced swimming in different biological media

To demonstrate the mechanism of propulsion of the PHI microswimmers, the light from a photodiode was focused with an intensity of 1.9 W/cm^2 at 385 nm on the particle chamber. The mean speed of the illuminated microswimmers in deionized (DI) water was 24.2 ± 1.9 μm/s (Fig. 2A and movie S1). In this case, their photocatalytically induced swimming is attributed to water oxidation and reduction of dissolved oxygen on the illuminated PHI hemisphere (*51*). To explore and determine the influence of different ionic and biological constituents on the propulsion efficiency of the PHI microswimmers, different pH neutral buffers and relevant biological media were tested (see note S1 for the ingredients and concentrations of all studied liquids). In brief, dPBS was used as the buffer solution for cell washing, which contains NaCl, KCl, Na_2HPO_4, and KH_2PO_4 at ca. 10 g/liter (~150 mM) in total. DMEM, commonly used to culture cells, contains the same salts (~160 mM), amino acids (ca. 2 g/liter, ~10 mM), and trace amounts of vitamins and glucose (4.5 g/liter, ~25 mM), some of which can be used as reducing agents and, hence, hole extraction fuel to power light-driven microswimmers (*52*). Under illumination, the mean speed of the microswimmers in dPBS was 19.0 ± 3.3 μm/s (21% slower than in DI water) and 23.7 ± 2.6 μm/s in DMEM (comparable with DI water), as seen in Fig. 2A. The ions present in dPBS (~150 mM) hence only have a relatively small influence on the speed of PHI, whereas the additional components in DMEM do not hamper the efficiency of photocatalytic reactions being responsible for the propulsion (movie S2). To emulate a realistic cell environment, the growth-supplementing medium fetal bovine serum (FBS) containing complex proteins and other components (*53*) was added to DMEM. The illuminated PHI microswimmers still moved with a mean speed of 12.5 ± 3.1 μm/s in DMEM medium with 10% FBS, hence 47% slower than in DMEM alone. This decrease in speed may be ascribed to the viscosity change and deposition of protein and other components on PHI, thus blocking surface reactions partially (*50*). In addition, a high concentration (1 M) of sodium phosphate buffer, an important component of DMEM, was also used to test the propulsion of PHI microswimmers. We observed a mean speed of 9.4 ± 1.7 μm/s, which is 54% lower than in the 160 mM salt containing DMEM. These findings show that PHI microswimmers can be used efficiently in many realistic biological environments and in salt solutions at concentrations even beyond those of biological fluids.

Active motion in heterogeneous and complex biological fluids, such as blood, is also crucial for future biomedical applications inside the human body. To test the propulsion capability of the PHI microswimmers in blood, they were mixed with blood cells with a 25% hematocrit (in DMEM medium), which is in the physiological range. When illuminated with ultraviolet (UV) light (385 nm), the PHI microswimmers also moved in the diluted red blood cell (RBC) solution. Autofluorescence of the PHI microswimmers, i.e., the intrinsic emission of PHI without any fluorescent markers, enabled their label-free imaging and detection even in the optically dense RBC solution. The mean speed of the PHI microswimmers in the dilute RBC solution, where viscosity remains the same in comparison with pure DMEM solution (*54*), was 20.2 ± 0.8 μm/s, also comparable with their mean speed in DMEM. The RBCs in the solution were also observed to be moving in the same direction, which appears to be caused by the fluidic flow arising from the collective propulsion of PHI microswimmers (note S2). The PHI microswimmers were not able to swim in whole blood, which could be ascribed to the increased viscosity and heterogeneous non-Newtonian nature making photocatalytically driven effective swimming impossible. A comparison of the available literature and the current work on ionic swimming is shown in table S1. For better comparison, a discussion of the wavelength and intensity dependence of the propulsion can be found in note S2, figs. S1 and S2, and tables S2 to S4. In DMEM, light-driven propulsion was efficient and proportional to the intensities in the UV and blue light, as shown in Fig. 2B.

Ionic tolerance for light-induced propulsion with NaCl

To better understand the ionic tolerance of PHI, the microswimmers were exposed to various NaCl concentrations and compared with the "sister material" melon under 385-nm illumination, as shown in Fig. 2C. In comparison with DI water (24.2 ± 1.9 μm/s), the PHI swimmers showed a 25% decreased speed (18.1 ± 3.4 μm/s) at 1 mM NaCl, with no obvious further decrease in speed observed until 100 mM (18.6 ± 3.4 μm/s). Changing the electrolyte cation to potassium at the same concentration (100 mM KCl) has negligible influence on the propulsion speed within the margin of error (20.7 ± 3.5 μm/s). At 1 M NaCl, they showed a further decrease (12%) in speed (16.1 ± 3.9 μm/s) (see movie S3). Hence, the speed was reduced only by 33% with respect to DI water and the characteristic EI50 is not yet reached. Only at 5 M NaCl, the speed is reduced to 9.7 ± 2.4 μm/s (60% less than the speed in DI water), surpassing the EI50. Hence, PHI's ion tolerance surpasses all reported light-driven microswimmers by two orders of magnitude, as summarized in table S1, and maintains fast light-induced propulsion even at 5 M salt concentrations.

We attribute the constant speed between 1 and 100 mM to a constantly high ionic mobility between the PHI microswimmer and ionic environment, which only becomes limiting at higher concentrations. To further investigate the effect of textural porosity on the high ion tolerance, PHI and melon were tested under identical conditions. Although both melon and PHI exhibit textural porosity [see Fig. 1A and figs. S7 and S8 for SEM and Brunauer-Emmett-Teller (BET) measurements], melon has no structural porosity because it consists of close-packed 1D heptazine imide chains, hence enabling only surface ionic interactions. The mean speed of the melon microswimmers under UV illumination was 11.7 ± 2.9 μm/s in DI water (43% lower than PHI). At 10 mM NaCl, the propulsion speed decreased weakly (9%), with EI50 being reached at ~100 mM (6 ± 1.3 μm/s). These findings also show that this 1D form of CN_x has a high ion tolerance (higher than any other material reported except PHI), which we tentatively attribute to its textural porosity, enabling ionic permeation by an internal flow of ions and liquid under illumination (*42*, *43*). However, at 1 M NaCl, the melon microswimmers

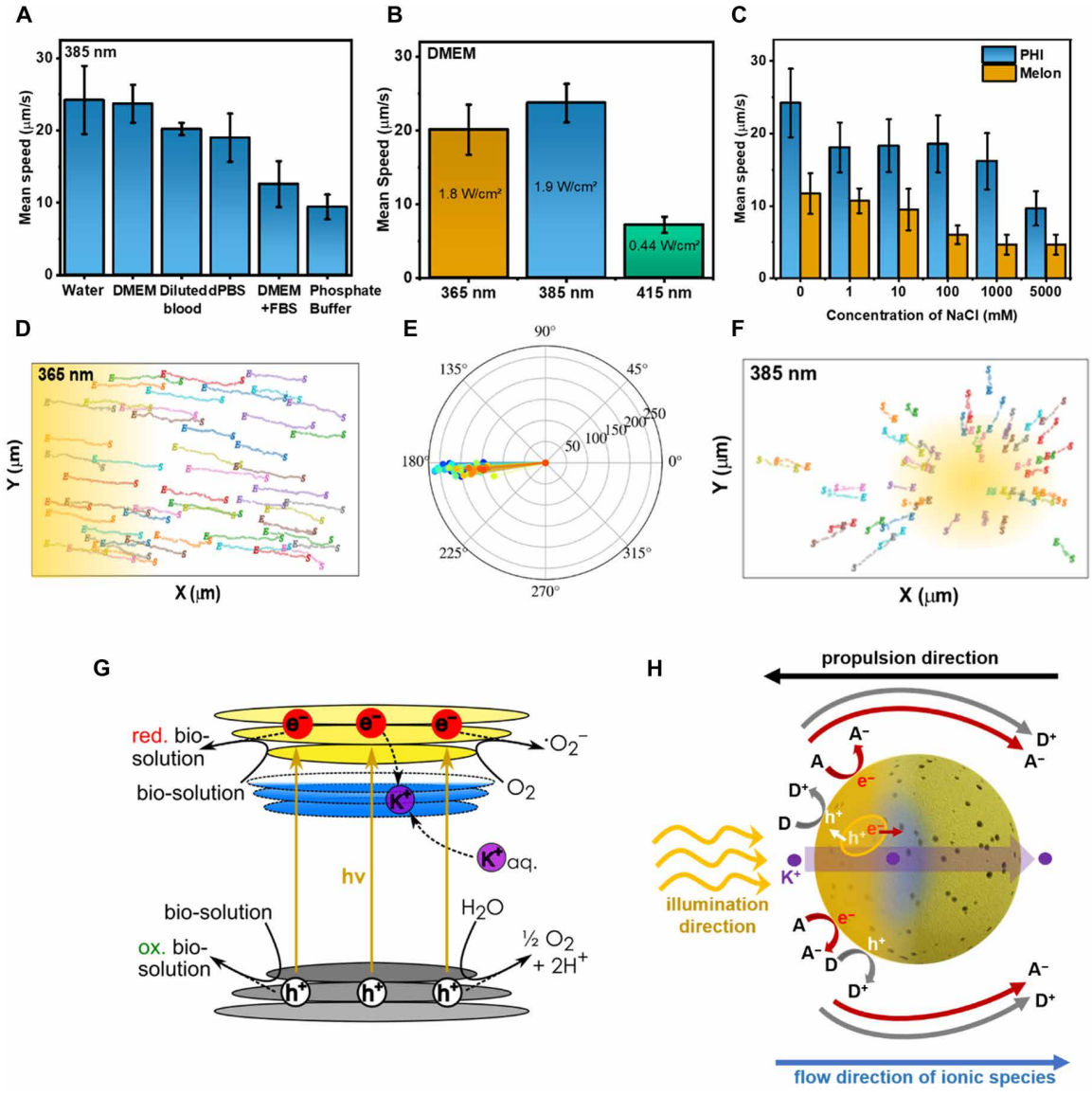

Fig. 2. PHI microswimmer propulsion in different ionic fluids. (**A**) Mean speeds ($N = 50$) of PHI microswimmers in various biological media (30 μg/ml) swimming under 385-nm light illumination, and the error bars indicate the SD in all plots. (**B**) Mean speeds ($N = 50$) of the PHI microswimmers in DMEM medium under different illumination wavelengths. The propulsion speed is constant under dilute (3 μg/ml) and under normal conditions (30 μg/ml). (**C**) Mean speed ($N = 50$) of the PHI and melon CN_x swimmers in increasing concentrations of NaCl under 385-nm illumination. (**D**) Sample 2D trajectories of the PHI microswimmers in DMEM medium swimming under 365-nm illumination from the side with S and E indicating the start and end of trajectories, showing a positive phototactic behavior. (**E**) Polar plot of the directed propulsion of the PHI microswimmers under the same conditions as (D) after 15 s of illumination. Radial scale bar, 50 μm. (**F**) Phototactic behavior of PHI microswimmers in DMEM medium swimming under 385-nm illumination from the bottom to a point in the image. S and E indicate the start and end of the trajectories. (**G**) Schematics of the band structure of PHI along with the reduction and oxidation reactions responsible for the photocatalytic propulsion of PHI microswimmers and the light-induced intercalation of alkali metal ions (K^+ or Na^+, e.g., purple) into the particle, enabled by optoionic effects assisting photocharging in PHI (blue). (**H**) Proposed mechanism for the phototactic propulsion of porous CN_x particles (nanopores not to the real scale and density; particle shape not perfectly spherical in reality) caused by asymmetric illumination and photocatalysis, resulting in ion flow around and through the particle. The movement of cations (purple) into and through the particle's pores counteracts the Debye layer collapse and enables ionic tolerance. Pseudocapacitive photocharging effects (blue) present in PHI increase ionic tolerance with respect to melon. Here, A and D represent electron donor and acceptor reactions, respectively. Also, h^+ and e^- represent the holes and electrons, respectively.

stopped ballistic swimming (only active Brownian motion was observed), which may be attributed to the absence of optoionic properties and a smaller thermodynamic driving force for oxidation (Fig. 1D).

In contrast to melon, PHI has not only textural but also structural nanopores, with a radius on the order of 3.84 Å (*44*, *45*, *47*). The pores are large enough to host and allow the passage of hydrated K^+ and Na^+ ions (hydrodynamic radius of 1.25 and 1.84 Å, respectively), making the molecular backbone of PHI permeable to ions. We have demonstrated in earlier work that the light-induced hole extraction and photo-charging ability of PHI is intimately linked to the presence of ions in the pores of PHI and the surrounding electrolyte, which may lead to light-induced ion transport throughout the structural

and textural nanopores of PHI and thus the movement of ions toward the (photogenerated) electrons on PHI (*42*, *45*, *46*, *48*), as illustrated in Fig. 2 (G and H). We believe it is these intrinsic optoionic properties of PHI, which are absent in melon, paired with porosity, that lead to sustained motion in high ionic strength media on the time scale of the experiments. The presence of both textural and structural pores invalidates the assumption of a hard sphere (the latter excluding liquid or ion flow through the volume of the particle), which is commonly used to describe phoresis. Hence, the Helmholtz-Smoluchowski equation, $U = \mu_e E_0$, where μ_e is the electrophoretic mobility and E_0 is the magnitude of the electric field, cannot be used to sufficiently describe the motion. Therefore, different theoretical models are needed to be developed in the future to fully capture the reason for the high ion tolerance of this organic semiconductor.

Despite the presence of ions and no dedicated fuel, the speed of light-driven PHI microswimmers (9 to 23 μm/s) is comparable with, and even higher, than the speed of other light-driven swimmers in absence of ions and in presence of dedicated fuels (5 to 25 μm/s) (*22*, *55*). The limitations on phoresis arising from the accumulation of ions around the particle are shown to be efficiently bypassed by suitable porosity, and in addition, it is hypothesized that optoionic effects enabling ion transport increase the ionic tolerance and speed of the swimmers. In the presence of buffers and biological fluidic media, the additional species partially negate the speed reduction, presumably by offering additional redox reaction pathways with respect to water and NaCl, hence increasing the efficiency of the photocatalytic propulsion process.

Phototaxis of the PHI microswimmers

Light-induced propulsion itself lacks directional control. However, phototactic properties of the microswimmers and light illumination direction control enable their steering to a desired location, which is very beneficial for their biomedical and other practical applications. To test possible phototactic properties of the PHI particles, they were illuminated with 365-nm UV light at a 45° angle from one side, with an intensity of 115 ± 15 mW/cm^2, in DMEM medium. This created a light gradient along the *x* axis as shown in Fig. 2D, which the particles followed. The mean speed of the microswimmers was 12.5 ± 0.4 μm/s in this case, which is substantially higher (78%) compared with the lateral motion measurement with the perpendicular illumination through the microscope objective at 400 mW/cm^2 (6.5 ± 1.2 μm/s), and hence as fast as with 10× stronger illumination from the bottom (1.2 W/cm^2). This apparent increase in speed is attributed to a change in directional component of the measured speed. In the case of illumination from the side, there was a larger parallel component resulting in a higher lateral speed; when illuminating from the bottom, the parallel component was slower, whereas the *z* component (parallel to the illumination) could not be analyzed, resulting in a lower effective speed. Besides, tumbling and rotational motion may cause a sidewise motion with the perpendicular illumination (*21*). As can be seen from the trajectories in Fig. 2D, the polar plot in Fig. 2E, and movie S4, the PHI particles followed the direction of illumination very precisely; also, the speed was not affected by decreasing the particle concentration to very dilute cases (from 30 to 3 μg/ml). At 415-nm side illumination, the same phototactic behavior resulted, with a speed of 5.3 ± 1.3 μg/ml. When the direction of illumination was changed, the direction of swimming also changed, as shown in movie S4. This behavior could be explained by the illumination from one side only, shadowing the other half of the particle, resulting in the creation of an artificial Janus-type structure that breaks the microswimmer's symmetry, independent of the irregular size and shape of the swimmers. The negative zeta potential of PHI (−35 mV as measured in 10 mM NaCl) (*44*) led to positive phototaxis in this situation (*22*, *56*–*58*).

When PHI microswimmers were illuminated under the optical microscope with light focused onto the image plane, the particles moved toward the middle of the light beam (Fig. 2F and movie S1), enabling collective assembly in one direction. Further effects and possible thermal contributions in the case of dense suspensions are discussed in note S3, and figs. S4 to S6 show control experiments with nonpropelled, passive polystyrene particles. The propulsion under these conditions was shown to last for 2 hours with minimal speed reduction (−18%, from 23.5 ± 3.5 to 19.8 ± 3.2 μm/s), attributed to crowding and shading (fig. S7). The phototactic properties of the PHI microswimmers, which originate predominantly from their light-induced photocatalytic propulsion (Fig. 2, G and H, and movie S4), as evidenced most directly by the propulsion at low particle concentrations and the decreasing speed with increasing ionic concentration, can be used to control the direction of their motion in various future biomedical applications, such as targeted drug delivery and cargo transport. Besides, thermal effects can assist the swarming behavior under crowded conditions. Phototactic swimming of microswimmers in curvilinear paths and complex paths can be demonstrated by moving the light source dynamically with respect to the swimmers, thereby changing the illumination angle. The swimming in curvilinear paths is essential for applications such as cargo transport, where the swimmer would need to navigate against obstacles. Such phototactic swimming is shown in fig. S8 and movie S6.

Cytotoxicity tests

A low cytotoxicity profile of the microswimmers is an essential requirement for their future biomedical applications. Therefore, we tested the cytotoxicity of the PHI microswimmers with a normal cell line (NIH 3T3 fibroblast cells) and two cancer cell lines (HT-29 colorectal cancer cells and SKBR3 breast cancer cells). Live/dead staining of the tested cell lines incubated with varying concentrations of PHI microswimmers (0 to 30 μg/ml) for 24 hours showed no decrease in cell viability for all cell lines (Fig. 3, A and B). Other than particle cytotoxicity, we also tested the effect of illumination and catalytic activity of PHI microswimmers on cellular viability. Illumination at 415 nm (440 mW/cm^2) and 385 nm (1.1 W/cm^2) of a high density of PHI microswimmers (30 μg/ml) on the fibroblast cells for varying durations (0 to 30 min) showed no negative effects on their viability immediately after testing (Fig. 3, C and D). Coupled to the efficient propulsion of the PHI microswimmers in biological media, their operation in cellular environments is highly promising. When illuminated at 415 nm for 30 min, the cells retained viability up to 24 hours. With 385-nm UV light, 24-hour viability is retained up to 10-min illumination. Because strong UV illumination for long durations is harmful for the cells (*59*), they are not viable if illumination lasts for 30 min. Studies with primary cells from mouse splenocytes further confirmed that there was no detectable level of interleukin-12 (IL-12; proinflammatory marker) in either of the untreated samples in concentrations used above in the dark. As shown here, long-duration exposure to short wavelength light can cause damage to the cells; therefore, the swimmer

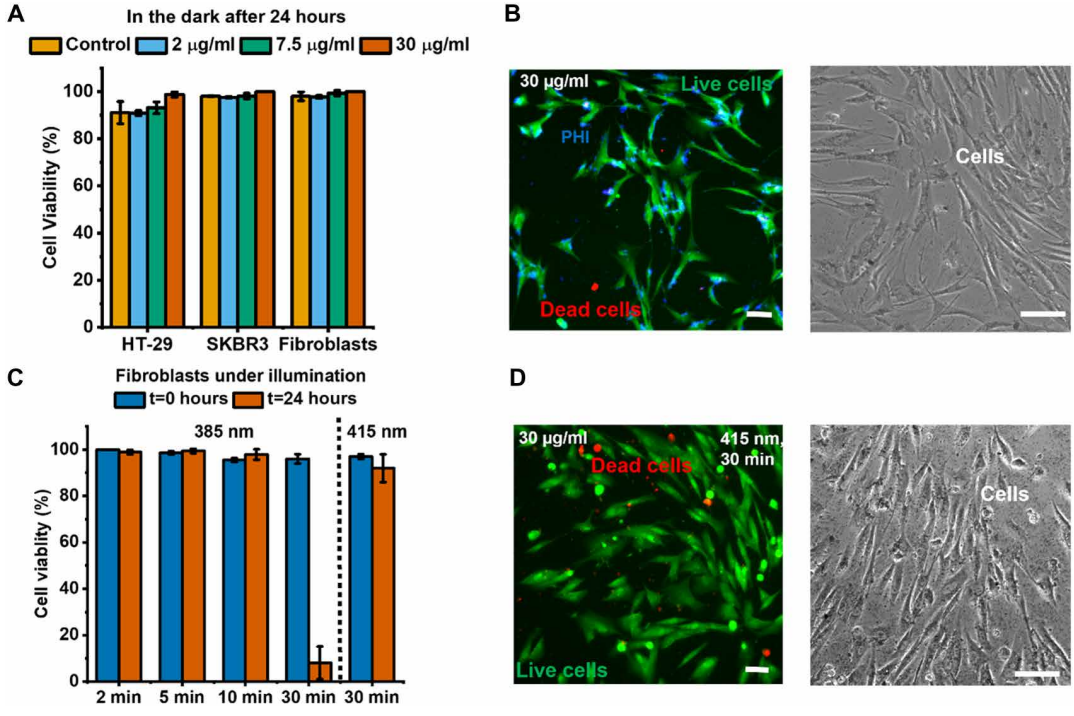

Fig. 3. Cytotoxicity of the PHI microswimmers. (**A**) Cell viability of fibroblasts and cancer cells incubated with the PHI microswimmers at varying concentrations after 24 hours. Data represent the means and the error bars represent the SD of ~300 cells. (**B**) Live/dead staining of healthy BJ human fibroblast cells after 24 hours of incubation with the PHI microswimmers. Green and red indicates the live cells and dead cells, respectively, along with the bright-field images in the same conditions indicating the cells and PHI (black dots). Scale bars, 100 μm. (**C**) Cell viability of BJ fibroblast cells in presence of PHI microswimmers (30 μg/ml) right after and 24 hours after illumination for varying durations at 385 nm and 415 nm. Data represent means ± SD. (**D**) Live/dead staining of BJ fibroblast cells after swimming of PHI swimmers, not in the picture (30 μg/ml), via light (415 nm) after 30 min, along with the bright-field images under the same conditions indicating the cells and PHI (black dots). Scale bars, 100 μm.

exposure times need to be limited to 10 min only for 385-nm wavelength light, whereas it can last 30 min or more for 415-nm wavelength light. Such durations are typically long enough for the desired in vitro or in vivo biomedical functionalities. In vivo studies are required as future work for validating the complete biocompatibility of the PHI microswimmers; however, the cytotoxicity and immunogenicity experiments are important steps in this direction.

Drug loading and hypoxically, pH-, and light-triggered drug release

Biocompatible PHI microswimmers are capable of actively carrying and releasing drugs and other cargos attached to their porous body structure at a target location. The concept of their targeted drug delivery is illustrated in Fig. 4A with an anticancer model drug, doxorubicin (DOX). The presence of textural nanopores in both PHI and melon microswimmers is beneficial for enhanced drug loading efficiency (BET surface area is ~13 and 26 m^2/g and pore size distribution is from 5 to 20 nm and 5 to 40 nm for the PHI and melon microswimmers, respectively; see fig. S9 and note S4), enabling the adsorption of drugs within the microparticle pores (*44*, *60*). We further anticipate that drug uptake is assisted by the amine surface groups of both CN_x, enabling hydrogen bonding interactions with the drug, and by the negative zeta potential of melon and especially PHI, which intrinsically attracts the positively charged DOX molecules at pH 7 (*44*, *60*, *61*). To test this hypothesis, 200 μg of DOX was added to a suspension of 100 μg of PHI microswimmers dispersed in 1 ml of DMEM, resulting in 185 μg of DOX encapsulated with a DOX loading efficiency of 185% on PHI after 24 hours, which is far higher than previously reported values of 20 to 70% (*62*–*64*). Figure 4B shows the fluorescence image of DOX loaded on the PHI particles. For melon, a loading efficiency of 110% (110 μg) resulted under the same conditions. Astonishingly, no passive release was observed for PHI in the absence of illumination for more than 30 days, even at room temperature. The stronger attachment and higher loading of DOX to the surface of PHI is likely due to enhanced interactions between the oxygen-rich DOX backbone and PHI, due to its more negative zeta potential in comparison to melon (*44*, *45*, *61*). Moreover, the DOX molecules loaded on PHI particles did not show a strong negative effect on the propulsion speed of the loaded PHI microswimmers in DMEM (18.5 ± 0.9 μm/s, 22% less than the speed in DI water). This can be rationalized by the fact that the large DOX molecules are predominantly physisorbed in the particle volume, rather than in the structural pores or on the outer particle surface, which does not significantly block the ion flow through the inner structure or affect the outer surface photocatalytic reactions of PHI with the surrounding medium that give rise to a field gradient around the particle and, hence, swimming propulsion. On the other hand, the speed reduction with loaded DOX again underlines that porosity and permeability for ions seem to be important parameters to enable propulsion in ionic media.

Illuminating the PHI and melon particles triggers the release of DOX, thus enabling a fully controlled, on-demand release of the drug. We used a 415-nm blue light at an intensity of 170 mW/cm^2 to study the release of DOX and related products from the microswimmers in both ambient and O_2-free environments (Fig. 4C and fig. S11A). Bandgap illumination of PHI microswimmers in oxygen-deficient suspensions triggers (oxidative) photocharging of the material, which is accompanied by a change of optoelectronic properties and a color change from yellow to blue (*47*, *49*). Hence, this charging effect is expected to influence the release, too (Fig. 4A). The charging effect was also observed for denser PHI suspensions

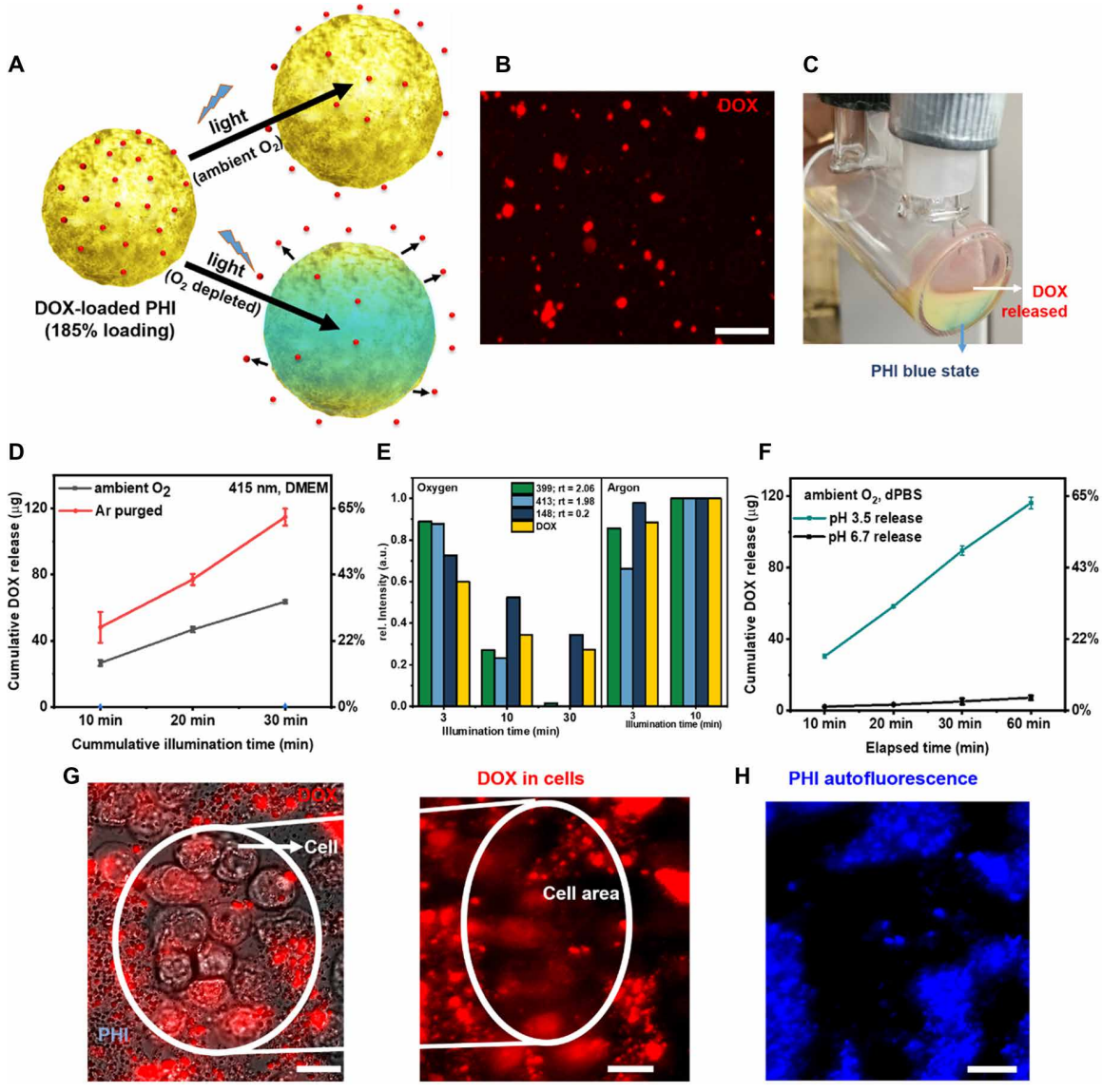

Fig. 4. Drug loading and hypoxically, light-, and pH-triggered drug release with the PHI microswimmers. (**A**) Schematic drug loading (DOX) and triggered release from the PHI microswimmers under ambient and hypoxic conditions. (**B**) Map of the DOX-loaded PHI microswimmers [185 μg/ml of DOX in PHI (100 μg/ml)] showing DOX fluorescence emission at 595 nm. Scale bar, 10 μm. (**C**) Photo of the DOX-loaded PHI microswimmers immediately after 30 min of illumination under oxygen-deficient conditions showing the charged blue state of PHI and the released DOX and by-products in red color. (**D**) Light-triggered cumulative release signal of DOX and by-products in DMEM medium at different time points under 415-nm illumination, with the supernatant being removed at each interval in ambient (black) and Ar-purged (red). The noncumulative release data are shown in fig. S12, and the error bars indicate the SD of $N = 3$ samples. (**E**) HPLC analysis of the main products found after photocatalytic DOX release from the PHI microswimmer in ambient and Ar-purged conditions at different illumination times, normalized to the highest signal of the DOX that was observed from the HPLC (see note S6 for the details). (**F**) pH-triggered release of DOX in PBS medium at pH 3.5 (green) with 54% of DOX being released after 60 min versus control (pH 6.7, black) showing negligible (~2%) release. (**G**) Optical microscopy (bright-field image) and fluorescence overlaid images of SKBR cancer cells (indicated within the circle) with preloaded PHI microswimmers under 415-nm illumination for 20 min showing released DOX uptake by the cells under emission at 595-nm fluorescence in red. (**H**) PHI autofluorescence image at 470 nm showing the PHI microswimmers adhering to the cancer cells after some amount of DOX release. The two fluorescent images are taken from the same frame. Scale bars in (G) and (H), 10 μm.

in DMEM even under ambient conditions (i.e., in the presence of oxygen), which appears to originate from photocatalytic oxygen consumption near the PHI surface (fig. S11B and note S5). The cumulative release signal of DOX from PHI in DMEM is shown in Fig. 4D for 3-, 10-, and 30-min intervals of illumination in both ambient and O_2-free environments. Results of the DOX release with continuous illumination are shown in fig. S12. Under ambient conditions, an optical equivalent of about 26 μg (14%) was released every 10 min, with 64 μg (35%) in 30 min cumulatively. When the amount of oxygen is decreased by purging the suspension with argon (Ar) 5 min before and during the illumination, enabling photocharging of PHI, an increase (almost doubling) in stepwise and cumulative release was observed, resulting in 114.8 ± 5.2 μg (62%) of DOX equivalently being released after 30 min (Fig. 4, C and D).

Tumor cells have oxygen-deficient, i.e., hypoxic, regions. Hence, a microswimmer that releases drugs faster in oxygen-deficient conditions is not only beneficial but could also be used in a theranostic sense for hypoxically triggered drug delivery in tumor regions.

For melon, a light-triggered and rather constant DOX release was also observed after 3 and 10 min of illumination, although at lower overall amounts than for PHI, although at similar proportions (~17 mg of DOX equivalent, 15% of loading and hence significantly less than 67% release possible with PHI despite higher initial loading), and with no significant differences under oxygen-depleted conditions for these short time scales (fig. S13).

Upon longer illumination however, beyond 60-min illumination time intervals, the DOX amount released from PHI was reduced under ambient (O_2-rich) conditions, suggesting a light-triggered degradation process, similar to observations made on DOX-loaded TiO_2 microparticles (*65*). Because degraded products of DOX show similar fluorescence and absorption bands, a further examination of the release products was only possible qualitatively by separation and mass spectroscopy (MS), which was realized by high-performance liquid chromatography–MS (HPLC-MS) analysis of the supernatants after release. Besides pristine DOX, modified DOX by-products were indeed observed after release (Fig. 4E and fig. S14). The dominant decomposition products have masses of m/z = 413, 399 and 148 (see scheme S1 for visualization of the reaction; more information on the drug release behavior is discussed in note S6). This gives evidence that not only the release of DOX itself but also of its oxidation products, which can act even more effectively on cells (*65*), can be intentionally tuned by the illumination time while being responsive to the presence of oxygen.

Besides, the PHI microswimmers are sensitive to acidic pH levels. A low pH triggers protonation of the PHI backbone and an increase in zeta potential, hence repelling the DOX (*45*, *61*). Within 60 min at pH 3.5, induced by adding HCl to PBS, the microswimmers released the loaded DOX (116.2 ± 3.3 μg, 63%) without any light illumination (control) as shown in Fig. 4F. In comparison, the control (pH 6.7) showed negligible release of ~2%, within the margins of instrumental error.

Next, the ability of PHI microswimmers to deliver DOX or its active modifications to cancer cells under illumination was studied to provide a proof of concept. The bright-field image of PHI microswimmers in a dense environment of cancer cells after 20-min illumination (415 nm) is shown in Fig. 4G. DOX or related products (red color) were released from the PHI microswimmers and taken up by the cancer cells after 24 hours of incubation; some amounts also diffused through the medium. Subsequently, the incubated cells died. The fluorescence image of the PHI microswimmers shows that the microswimmers stayed in the vicinity of the cancer cells (Fig. 4H) (*66*). This demonstrates that PHI microswimmers serve as smart light-driven cargo delivering agents under biological conditions. Their stimuli-responsive behavior triggers a theranostic function, making use of an intrinsic sensing property (i.e., charge accumulation enabled in oxygen-poor environments) that triggers an enhanced release of the therapeutic agents.

CONCLUSION

We have developed highly efficient carbon-based PHI microswimmers that can be propelled phototactically with light in aqueous salt media with high molarity (up to 5 M NaCl) and realistic biological cell media, such as dPBS, DMEM, DMEM/FBS, and diluted blood, without any additional fuel. Such particles exhibit positive phototaxis, which can be used to steer and locate the microswimmers into target locations (*18*) and can be photocharged even under oxygen-rich conditions. Their high ion tolerance for phototaxis (>5 M) is attributed to a favorable interplay between PHI's textural and structural porosity, as well as possible optoionic effects enabling ion motion into and through the particle, in the presence of high photocatalytic activity (*47*, *48*). As such, light-induced and controlled propulsion is realized without the need of dedicated particle morphology selection. Next, the biocompatibility of the PHI swimmers was verified with three different cell lines without and with visible light illumination and primary cells. Besides, because of their textural porosity, PHI microswimmers are shown to have a very high capacity for drug uptake (~185% of their own mass using the example of the anticancer drug DOX), which stays bound stably to the particle over a month, until a fast release is triggered by a pH change or bandgap illumination. Intriguingly, PHI shows stimuli-responsive drug release, because the release can be enhanced or modified by the intrinsic memristive photocharging ability under oxygen-deficient conditions, which are prevalent in hypoxic tumor regions, thus enabling potential future neuromorphic or theranostic applications (*48*, *67*–*70*). In addition to the multiple-stimuli responsive drug-release capability of the PHI microswimmers, we demonstrate their swimming and ease of tracking in crowded heterogeneous biological fluids, such as diluted blood, by monitoring PHI's inherent autofluorescence. These capabilities make the PHI microswimmers promising candidates for future in vitro and in vivo biomedical applications in hypoxic tumor regions inside the human body and organ-on-a-chip devices. Light penetration into tissues is a challenge for all previous and our light-driven microswimmers for in vivo deep-tissue medical applications because short wavelength light cannot penetrate the tissue. To overcome this challenge, long wavelength near-infrared light-driven microswimmers need to be developed in the future, which could penetrate several centimeters deep into the tissues. Moreover, in specific potential medical applications, a light source might be provided in deep regions by a catheter that could also deploy the microswimmers in a target location. Because of PHI's organic nature, we envision that the microswimmers can be further optimized for tailored surface functionalities and catalytic, morphological, and optical properties (*45*, *50*), opening up different avenues for smart responsive micromachines and theranostics in the future.

MATERIALS AND METHODS

PHI synthesis

PHI was synthesized according to a procedure described in the literature (*44*). Shortly, melamine (5.0 g) was heated in a tube furnace in a quartz glass boat to 550°C for 12 hours with a heating rate of 5°C/min under Ar flow. After cooling to ambient temperature, a yellow powder (2.0 to 2.5 g) was obtained. A total of 1.5 g of this product (melon) were thoroughly ground with KSCN (3.0 g), which was heated overnight to 140°C in vacuum to evaporate water. The mixture was heated in a tube furnace in an Alox boat to 400°C for 1 hour and 500°C for 30 min with a heating rate of 30°C/min under Ar flow. The Alox boat with the CN_x was sonicated two times for 15 min in 80 ml of water to disperse the yellow product. This suspension was washed six times with DI water by centrifugation

(20,000 rpm). The insoluble product was dried in vacuum at 60°C overnight.

SEM images of the microswimmers were captured by a Zeiss Merlin SEM. To capture the swimming of the microswimmers, a Zeiss Axio A1 inverted optical microscope was used. A Thorlabs M365L2 (Germany) UV lamp, Zeiss Colibri fluorescence source, and Thorlabs M415 were used for illumination through the inverted microscope. The videos were recorded from the microscope using a LD Plan-NeoFluar 40× objective lens and Axiocam 503 charge-coupled device camera at 62 frames/s. The swimming behavior of the microswimmers was systematically investigated by 2D mean square displacement (MSD) analysis on the captured videos for 15 s using a custom MATLAB and Python code.

The absorptance spectra of these samples were measured with a double monochromator spectrophotometer (Edinburgh Instruments, FLS-980). The measurements were performed locating the sample in the center of an integrating sphere attached to FLS-980 working in synchronous mode to discern any photoluminescence signal from the PHI particle. The sample suspension was measured in degassed, aqueous solution while simultaneously being stirred to prevent sedimentation.

The intensity of the illumination in the microscope was measured at the place of the sample chamber with a calibrated Ocean Optics OCEAN-FX-XR1-ES spectrophotometer after attenuation by a neutral density filter and integration of the spectral irradiance. The results have been normalized to the filter attenuation and to the spot size of the light beam in the microscope, which was measured to be 2.0 ± 0.5 mm in diameter, resulting in a relative experimental error of 50% after the error propagation calculation. For side illumination with the 365-nm diode, the light intensity was directly measured by a Thorlabs S310C/PM100D power meter.

Cytotoxicity tests

Human colorectal cancer cells, human breast cancer cells, and murine fibroblasts (American Type Culture Collection, Manassas, VA) were grown in DMEM supplemented with 10% (v/v) FBS and 1% (v/v) penicillin/streptomycin (Gibco, Grand Island, NY, USA) at 37°C in a 5% CO_2, 95% air-humidified atmosphere. Cells were reseeded after growing to confluence into µ-Slide eight-well plates (Ibidi GmbH, Gräfelfing, Germany) at a cell density of 25×10^3 cells per well and incubated for 2 days. For cytotoxicity testing, all three cell lines were incubated with PHI microswimmers at varying concentrations (0 to 30 µg/ml). Then, viability of difference cell lines was investigated using a LIVE/DEAD assay (Thermo Fisher Scientific, Waltham, MA) incorporating calcein-AM (green) and ethidium homodimer-1 (red) dyes. After 24 hours of incubation with the PHI microswimmers, live/dead cell viability was calculated from fluorescence microscopy images. Furthermore, cytotoxicity of microswimmers during light actuation (385 nm, 415 mW/cm^2) was tested by live/dead staining of fibroblast cells right after and 24 hours after actuation of PHI microswimmers for varying durations (0 to 10 min).

Cell culture

All cell culturing was performed under sterile conditions within a biosafety cabinet. The cell culture used for the isolated cells was composed of DMEM from Gibco. This was supplemented with 10% heat-inactivated FBS and 1% penicillin and streptomycin (Gibco). The storage condition for cells during incubation was an incubator set at 5% CO_2, ~90% humidity, and 37°C.

Cell isolation

Mouse spleen was provided by the Facility for Animal Welfare, Veterinary Service and Laboratory Animal Science at Eberhard Karl's University Tubingen. After mice were euthanized, the spleen was removed and kept on ice in PBS without Ca^{2+}/Mg^{2+} for transport to Max Planck Institute at Stuttgart. The spleen was forced through a cell strainer at 70 µm, also containing DMEM media. After filtering, the supernatant was centrifuged at 800*g* for 5 min. The upper layer of supernatant was removed, and the cells were washed with lysing buffer for RBCs removal. This occurred for 8 min at room temperature. Then, the cells were centrifuged and resuspended in fresh medium before being placed into six-well plates at 1 million cells per well. The chosen concentrations of the tested material were added to the wells for 24 hours before the medium was removed and frozen before enzyme-linked immunosorbent assay (ELISA) analysis.

ELISA protocol (IL-12)

A high affinity binding plate (Greiner) was coated with 100 µl of diluted, purified anticytokine capture antibody. The plate was sealed and incubated at 4°C overnight. The next day, the capture antibody was removed by decanting, and a blocking solution was added for 1 hour at room temperature. A series of washes was performed between each step. The samples and standards were added and incubated for 2 hours at room temperature. After rinsing, the working detector was added and incubated for 1 hour. The final rinse was performed, the substrate solution was added, and the plate was read after adding stop solution at 30 min.

Swimming in biofluids

DMEM, dPBS, and DMEM + FBS (Sigma-Aldrich) were used as purchased. The PHI swimmers were dispersed in the medium and illuminated inside a microfluidic chamber to measure their swimming.

Cancer drug DOX loading

The efficiency of loading was measured by centrifuging the DOX-loaded microswimmers and comparing the optical density (OD) of the supernatant with the precalibrated OD of DOX (200 µg/ml) at 480 nm. PHI (100 µg/ml) was dispersed with DOX (200 mg/ml), and this solution was stirred in dark for 24 hours to allow the DOX to be adsorbed. After 24 hours, the suspension was centrifuged, and the supernatant was used for measuring the DOX loading. The DOX-loaded PHI was washed three times with water and stored at 4°C for further delivery experiments. The DOX-loaded microswimmers were illuminated with 415-nm light at an intensity of 170 mW/cm^2 from the bottom in a cylindrical quartz glass stirring simultaneously (fig. S11A). To remove dissolved oxygen, the suspension was bubbled with Ar through a needle for 5 min before the illumination and during the respective illumination time. For the pH release, the pH of the resulting HCl-diluted PBS solution was checked using a pH meter to confirm the stability of the pH during the release experiments.

Sorption measurements

Sorption measurements were performed on a Quantachrome Instruments Autosorb iQ 3 with a coupled Cryosync for cooling and Ar as analysis gas at 87 K. The pore size distribution was determined from Ar adsorption isotherms using the NLDFT (cylindrical nanopores, adsorption branch) kernel in carbon for Ar at 87 K implemented in the ASiQwin software version 3.01. Samples were activated in high vacuum at 120°C for 12 hours before measurement.

HPLC-MS analysis

HPLC-MS was performed on an Agilent 1290 Infinity II LC system connected to an Agilent InfinityLab LC/MSD XT single quadrupole MS with a multimode ESI-APCI ionization source. Analysis of the combined signals was performed using MestReNova (version 14) software package with MS analysis tools. Chromatographic separation was achieved on an Agilent EclipsePlus C18 column (2.1 mm by 50 mm by 1.8 μm) at 40°C with mixtures of acetonitrile (MeCN), water, and formic acid, according to the solvent composition timetable (tables S5 and S6) and a total solvent flow of 0.7 ml/min. MS data were obtained using MM-APCI ionization (positive) and in selective ion monitoring (SIM) mode for signals mass/charge ratio (m/z) = 544.2 (DOX), 399.1, 413.1, and 148.1 (degradation products).

Sample preparation

After centrifugation of the particles, an aliquot of the supernatant (100 μl) was diluted with 400 μl of MeCN:water [80:20 (v/v)]. The diluted samples were filtered through a syringe filter [0.2 μm, polytetrafluoroethylene (PTFE)] and injected (5 μl) into the HPLC-MS.

Calibration

To determine the concentration of DOX quantitatively, a multilevel calibration of the mass signal (area, SIM) was performed with a concentration series (fig. S15 and table S5). An appropriate volume of stock solution of DOX (c = 1 mg/ml in water) was diluted with DMEM to prepare the samples C_1 to C_4. Then, an aliquot (15 μl) of the calibration sample was diluted with 985 μl of MeCN:water [80:20 (v/v)]. The diluted samples were filtered through a syringe filter (0.2 μm, PTFE) and injected (1 μl) into the HPLC-MS.

Quantification of DOX

The concentration of DOX in an unknown sample was calculated from the peak area of the mass trace measured in SIM mode (m/z = 544.18) as follows (see figs. S13 to S15 for calibration curve and chromatograms)

$$c(\mathrm{DOX}) = \frac{(\mathrm{Area} - 757.48508)}{42517.78309}\frac{\mathrm{mg}}{\mathrm{ml}}$$

which already includes the sample dilution factor (0.2) and injection volume (5 μl).

Statistics

All quantitative values were presented as means ± SD of the mean. For all mean speed plots, the number of microswimmers tracked was 50. In the case of the drug release, the number of samples was three, and for live/dead cell analysis, it was ~300 cells.

SUPPLEMENTARY MATERIALS

www.science.org/doi/10.1126/scirobotics.abm1421
Notes S1 to S6
Figs. S1 to S17
Scheme S1
Tables S1 to S6
Movies S1 to S6
References (*71*–*79*)

REFERENCES AND NOTES

1. M.Sitti, *Mobile Microrobotics* (MIT Press, 2017).
2. S. Sanchez, L. Soler, J. Katuri, Chemically powered micro- and nanomotors. *Angew. Chem. Int. Ed. Engl.* **54**, 1414–1444 (2015).
3. P. Erkoc, I. C. Yasa, H. Ceylan, O. Yasa, Y. Alapan, M. Sitti, Mobile microrobots for active therapeutic delivery. *Adv. Therapeutics* **2**, 1800064 (2019).
4. H. Eskandarloo, A. Kierulf, A. Abbaspourrad, Light-harvesting synthetic nano- and micromotors: A review. *Nanoscale* **9**, 12218–12230 (2017).
5. Y. Alapan, O. Yasa, B. Yigit, I. C. Yasa, P. Erkoc, M. Sitti, Microrobotics and microorganisms: Biohybrid autonomous cellular robots. *Ann. Rev. Control Robot. Autonom. Systs.* **2**, 205–230 (2019).
6. M. Luo, Y. Feng, T. Wang, J. Guan, Micro-/nanorobots at work in active drug delivery. *Adv. Funct. Mater.* **28**, 1706100 (2018).
7. X. Ma, S. Sánchez, Self-propelling micro-nanorobots: Challenges and future perspectives in nanomedicine. *Nanomedicine* **12**, 1363–1367 (2017).
8. J. Li, B. E.-F. de Ávila, W. Gao, L. Zhang, J. Wang, Micro/nanorobots for biomedicine: Delivery, surgery, sensing, and detoxification. *Sci. Robot.* **2**, eaam6431 (2017).
9. B. E.-F. de Ávila, P. Angsantikul, J. Li, M. Angel Lopez-Ramirez, D. E. Ramírez-Herrera, S. Thamphiwatana, C. Chen, J. Delezuk, R. Samakapiruk, V. Ramez, M. Obonyo, L. Zhang, J. Wang, Micromotor-enabled active drug delivery for in vivo treatment of stomach infection. *Nat. Commun.* **8**, 272 (2017).
10. Z. Wu, L. Li, Y. Yang, P. Hu, Y. Li, S.-Y. Yang, L. V. Wang, W. Gao, A microrobotic system guided by photoacoustic computed tomography for targeted navigation in intestines in vivo. *Sci. Robot.* **4**, eaax0613 (2019).
11. J. Wang, W. Gao, Nano/microscale motors: Biomedical opportunities and challenges. *ACS Nano* **6**, 5745–5751 (2012).
12. W. Gao, R. Dong, S. Thamphiwatana, J. Li, W. Gao, L. Zhang, J. Wang, Artificial micromotors in the mouse's stomach: A step toward in vivo use of synthetic motors. *ACS Nano* **9**, 117–123 (2015).
13. X. Ma, A. C. Hortelão, T. Patiño, S. Sánchez, Enzyme catalysis to power micro/nanomachines. *ACS Nano* **10**, 9111–9122 (2016).
14. A. Llopis-Lorente, A. García-Fernández, N. Murillo-Cremaes, A. C. Hortelão, T. Patiño, R. Villalonga, F. Sancenón, R. Martínez-Máñez, S. Sánchez, Enzyme-powered gated mesoporous silica nanomotors for on-command intracellular payload delivery. *ACS Nano* **13**, 12171–12183 (2019).
15. A. C. Hortelão, T. Patiño, A. Perez-Jiménez, À. Blanco, S. Sánchez, Enzyme-powered nanobots enhance anticancer drug delivery. *Adv. Funct. Mater.* **28**, 1705086 (2018).
16. H. Šípová-Jungová, D. Andrén, S. Jones, M. Käll, Nanoscale inorganic motors driven by light: Principles, realizations, and opportunities. *Chem. Rev.* **120**, 269–287 (2020).
17. L. Xu, F. Mou, H. Gong, M. Luo, J. Guan, Light-driven micro/nanomotors: From fundamentals to applications. *Chem. Soc. Rev.* **46**, 6905–6926 (2017).
18. J. Wang, Z. Xiong, J. Zheng, X. Zhan, J. Tang, Light-driven micro/nanomotor for promising biomedical tools: Principle, challenge, and prospect. *Acc. Chem. Res.* **51**, 1957–1965 (2018).
19. D. Zhang, Y. Sun, M. Li, H. Zhang, B. Song, B. Dong, A phototactic liquid micromotor. *J. Mater. Chem. C* **6**, 12234–12239 (2018).
20. L. Kong, C. C. Mayorga-Martinez, J. Guan, M. Pumera, Photocatalytic micromotors activated by UV to visible light for environmental remediation, micropumps, reversible assembly, transportation, and biomimicry. *Small* **16**, e1903179 (2019).
21. W. E. Uspal, Theory of light-activated catalytic Janus particles. *J. Chem. Phys.* **150**, 114903 (2019).
22. B. Dai, J. Wang, Z. Xiong, X. Zhan, W. Dai, C. C. Li, S. P. Feng, J. Tang, Programmable artificial phototactic microswimmer. *Nat. Nanotechnol.* **11**, 1087–1092 (2016).
23. M. You, C. Chen, L. Xu, F. Mou, J. Guan, Intelligent micro/nanomotors with taxis. *Acc. Chem. Res.* **51**, 3006–3014 (2018).
24. M. Kuron, P. Kreissl, C. Holm, Toward understanding of self-electrophoretic propulsion under realistic conditions: From bulk reactions to confinement effects. *Acc. Chem. Res.* **51**, 2998–3005 (2018).
25. J. L. Moran, J. D. Posner, Role of solution conductivity in reaction induced charge auto-electrophoresis. *Phys. Fluids* **26**, 042001 (2014).
26. A. Brown, W. Poon, Ionic effects in self-propelled Pt-coated Janus swimmers. *Soft Matter* **10**, 4016–4027 (2014).
27. V. Sridhar, B.-W. Park, S. Guo, P. A. van Aken, M. Sitti, Multiwavelength-steerable visible-light-driven magnetic CoO–TiO2 microswimmers. *ACS Appl. Mater. Interfaces* **12**, 24149–24155 (2020).
28. V. Sridhar, B.-W. Park, M. Sitti, Light-driven janus hollow mesoporous TiO2–Au microswimmers. *Adv. Funct. Mater.* **28**, 1704902 (2018).
29. X. Wang, V. Sridhar, S. Guo, N. Talebi, A. Miguel-López, K. Hahn, P. A. van Aken, S. Sánchez, Fuel-free nanocap-like motors actuated under visible light. *Adv. Funct. Mater.* **28**, 1705862 (2018).
30. X. Wang, L. Baraban, A. Nguyen, J. Ge, V. R. Misko, J. Tempere, F. Nori, P. Formanek, T. Huang, G. Cuniberti, J. Fassbender, D. Makarov, High-motility visible light-driven Ag/AgCl janus micromotors. *Small* **14**, e1803613 (2018).
31. J. Wang, Z. Xiong, X. Zhan, B. Dai, J. Zheng, J. Liu, J. Tang, A silicon nanowire as a spectrally tunable light-driven nanomotor. *Adv. Mater.* **29**, 1701451 (2017).

32. K. Villa, F. Novotny, J. Zelenka, M. P. Browne, T. Ruml, M. Pumera, Visible-light-driven single-component $BiVO_4$ micromotors with the autonomous ability for capturing microorganisms. *ACS Nano* **13**, 8135–8145 (2019).
33. J. G. Gibbs, Shape- and material-dependent self-propulsion of photocatalytic active colloids, interfacial effects, and dynamic interparticle interactions. *Langmuir* **36**, 6938–6947 (2020).
34. X. Zhan, J. Wang, Z. Xiong, X. Zhang, Y. Zhou, J. Zheng, J. Chen, S. P. Feng, J. Tang, Enhanced ion tolerance of electrokinetic locomotion in polyelectrolyte-coated microswimmer. *Nat. Commun.* **10**, 3921 (2019).
35. M. Wei, C. Zhou, J. Tang, W. Wang, Catalytic micromotors moving near polyelectrolyte-modified substrates: The roles of surface charges, morphology, and released ions. *ACS Appl. Mater. Interfaces* **10**, 2249–2252 (2018).
36. J. Palacci, S. Sacanna, S. H. Kim, G. R. Yi, D. J. Pine, P. M. Chaikin, Light-activated self-propelled colloids. *Philos. Trans. A Math. Phys. Eng. Sci.* **372**, 20130372 (2014).
37. Q. Wang, R. Dong, C. Wang, S. Xu, D. Chen, Y. Liang, B. Ren, W. Gao, Y. Cai, Glucose-fueled micromotors with highly efficient visible-light photocatalytic propulsion. *ACS Appl. Mater. Interfaces* **11**, 6201–6207 (2019).
38. A. Aziz, S. Pane, V. Iacovacci, N. Koukourakis, J. Czarske, A. Menciassi, M. Medina-Sánchez, O. G. Schmidt, Medical imaging of microrobots: Toward in vivo applications. *ACS Nano* **14**, 10865–10893 (2020).
39. V. W.-h. Lau, M. B. Mesch, V. Duppel, V. Blum, J. Senker, B. V. Lotsch, Low-molecular-weight carbon nitrides for solar hydrogen evolution. *J. Am. Chem. Soc.* **137**, 1064–1072 (2015).
40. X. Wang, K. Maeda, A. Thomas, K. Takanabe, G. Xin, J. M. Carlsson, K. Domen, M. Antonietti, A metal-free polymeric photocatalyst for hydrogen production from water under visible light. *Nat. Mater.* **8**, 76–80 (2009).
41. W.-J. Ong, L.-L. Tan, Y. H. Ng, S.-T. Yong, S.-P. Chai, Graphitic Carbon Nitride (g-C3N4)-based photocatalysts for artificial photosynthesis and environmental remediation: Are we a step closer to achieving sustainability? *Chem. Rev.* **116**, 7159–7329 (2016).
42. K. Xiao, L. Chen, R. Chen, T. Heil, S. D. C. Lemus, F. Fan, L. Wen, L. Jiang, M. Antonietti, Artificial light-driven ion pump for photoelectric energy conversion. *Nat. Commun.* **10**, 74 (2019).
43. K. Xiao, P. Giusto, L. Wen, L. Jiang, M. Antonietti, Nanofluidic ion transport and energy conversion through ultrathin free-standing polymeric carbon nitride membranes. *Angew. Chem. Int. Ed.* **57**, 10123–10126 (2018).
44. V. W.-h. Lau, I. Moudrakovski, T. Botari, S. Weinberger, M. B. Mesch, V. Duppel, J. Senker, V. Blum, B. V. Lotsch, Rational design of carbon nitride photocatalysts by identification of cyanamide defects as catalytically relevant sites. *Nat. Commun.* **7**, 12165 (2016).
45. H. Schlomberg, J. Kröger, G. Savasci, M. W. Terban, S. Bette, I. Moudrakovski, V. Duppel, F. Podjaski, R. Siegel, J. Senker, R. E. Dinnebier, C. Ochsenfeld, B. V. Lotsch, Structural insights into poly(heptazine imides): A light-storing carbon nitride material for dark photocatalysis. *Chem. Mater.* **31**, 7478–7486 (2019).
46. A. Savateev, S. Pronkin, M. G. Willinger, M. Antonietti, D. Dontsova, Towards organic zeolites and inclusion catalysts: Heptazine imide salts can exchange metal cations in the solid state. *Chem. Asian J.* **12**, 1517–1522 (2017).
47. F. Podjaski, J. Kroger, B. V. Lotsch, Toward an aqueous solar battery: Direct electrochemical storage of solar energy in carbon nitrides. *Adv. Mater.* **30**, 1705477 (2018).
48. F. Podjaski, B. V. Lotsch, Optoelectronics meets optoionics: Light storing carbon nitrides and beyond. *Adv. Energy Mater.* **11**, 2003049 (2021).
49. V. W.-h. Lau, D. Klose, H. Kasap, F. Podjaski, M.-C. Pignié, E. Reisner, G. Jeschke, B. V. Lotsch, Dark photocatalysis: Storage of solar energy in carbon nitride for time-delayed hydrogen generation. *Angew. Chem. Int. Ed. Engl.* **56**, 510–514 (2017).
50. J. Kröger, A. Jiménez-Solano, G. Savasci, P. Rovó, I. Moudrakovski, K. Küster, H. Schlomberg, H. A. Vignolo-González, V. Duppel, L. Grunenberg, C. B. Dayan, M. Sitti, F. Podjaski, C. Ochsenfeld, B. V. Lotsch, Interfacial engineering for improved photocatalysis in a charge storing 2D carbon nitride: Melamine functionalized poly(heptazine imide). *Adv. Energy Mater.* **11**, 2003016 (2020).
51. V. Sridhar, F. Podjaski, J. Kröger, A. Jiménez-Solano, B.-W. Park, B. V. Lotsch, M. Sitti, Carbon nitride-based light-driven microswimmers with intrinsic photocharging ability. *Proc. Natl. Acad. Sci.* **117**, 24748–24756 (2020).
52. M. Pacheco, B. Jurado-Sanchez, A. Escarpa, Visible-light-driven janus microvehicles in biological media. *Angew. Chem. Int. Ed. Engl.* **58**, 18017–18024 (2019).
53. K. V. Honn, J. A. Singley, W. Chavin, Fetal bovine serum: A multivariate standard. *Proc. Soc. Exp. Biol. Med.* **149**, 344–347 (1975).
54. M. Singh, N. A. Coulter, Rheology of blood: Effect of dilution with various dextrans. *Microvasc. Res.* **5**, 123–130 (1973).
55. H. Qin, X. Wu, X. Xue, H. Liu, Light actuated swarming and breathing-like motion of graphene oxide colloidal particles. *Commun. Chem.* **1**, 72 (2018).
56. J. Wang, H. Wu, X. Liu, Q. Liang, Z. Bi, Z. Wang, Y. Cai, R. Dong, Carbon-dot-induced acceleration of light-driven micromotors with inherent fluorescence. *Adv. Intell. Syst.* **2**, 1900159 (2020).
57. C. Chen, F. Mou, L. Xu, S. Wang, J. Guan, Z. Feng, Q. Wang, L. Kong, W. Li, J. Wang, Q. Zhang, Light-steered isotropic semiconductor micromotors. *Adv. Mater.* **29**, 1603374 (2017).
58. Y. Sun, J. Jiang, G. Zhang, N. Yuan, H. Zhang, B. Song, B. Dong, Visible light-driven micromotor with incident-angle-controlled motion and dynamic collective behavior. *Langmuir* **37**, 180–187 (2021).
59. S. J. Bryant, C. R. Nuttelman, K. S. Anseth, Cytocompatibility of UV and visible light photoinitiating systems on cultured NIH/3T3 fibroblasts in vitro. *J. Biomater. Sci. Polym. Ed.* **11**, 439–457 (2000).
60. Y. Gao, Y. Chen, X. Ji, X. He, Q. Yin, Z. Zhang, J. Shi, Y. Li, Controlled intracellular release of doxorubicin in multidrug-resistant cancer cells by tuning the shell-pore sizes of mesoporous silica nanoparticles. *ACS Nano* **5**, 9788–9798 (2011).
61. V. W.-h. Lau, V. W.-z. Yu, F. Ehrat, T. Botari, I. Moudrakovski, T. Simon, V. Duppel, E. Medina, J. K. Stolarczyk, J. Feldmann, V. Blum, B. V. Lotsch, Urea-modified carbon nitrides: Enhancing photocatalytic hydrogen evolution by rational defect engineering. *Adv. Energy Mater.* **7**, 1602251 (2017).
62. C. K. Schmidt, M. Medina-Sánchez, R. J. Edmondson, O. G. Schmidt, Engineering microrobots for targeted cancer therapies from a medical perspective. *Nat. Commun.* **11**, 5618 (2020).
63. B. Wang, K. Kostarelos, B. J. Nelson, L. Zhang, Trends in micro-/nanorobotics: Materials development, actuation, localization, and system integration for biomedical applications. *Adv. Mater.* **33**, 2002047 (2020).
64. J. Dong, Y. Zhao, K. Wang, H. Chen, L. Liu, B. Sun, M. Yang, L. Sun, Y. Wang, X. Yu, L. Dong, Fabrication of graphitic carbon nitride quantum dots and their application for simultaneous fluorescence imaging and pH-responsive drug release. *ChemistrySelect* **3**, 12696–12703 (2018).
65. P. Calza, C. Medana, M. Sarro, V. Rosato, R. Aigotti, C. Baiocchi, C. Minero, Photocatalytic degradation of selected anticancer drugs and identification of their transformation products in water by liquid chromatography–high resolution mass spectrometry. *J. Chromatogr. A* **1362**, 135–144 (2014).
66. W. Zhang, G. Dang, J. Dong, Y. Li, P. Jiao, M. Yang, X. Zou, Y. Cao, H. Ji, L. Dong, A multifunctional nanoplatform based on graphitic carbon nitride quantum dots for imaging-guided and tumor-targeted chemo-photodynamic combination therapy. *Colloids Surf. B Biointerfaces* **199**, 111549 (2021).
67. S. H. Jo, T. Chang, I. Ebong, B. B. Bhadviya, P. Mazumder, W. Lu, Nanoscale memristor device as synapse in neuromorphic systems. *Nano Lett.* **10**, 1297–1301 (2010).
68. J. Rivnay, S. Inal, A. Salleo, R. M. Owens, M. Berggren, G. G. Malliaras, Organic electrochemical transistors. *Nat. Rev. Mater.* **3**, 17086 (2018).
69. K. Xiao, C. Wan, L. Jiang, X. Chen, M. Antonietti, Bioinspired ionic sensory systems: The successor of electronics. *Adv. Mater.* **32**, 2000218 (2020).
70. A. Pérez-Tomás, Functional oxides for photoneuromorphic engineering: Toward a solar brain. *Adv. Mater. Interfaces* **6**, 1900471 (2019).
71. I. V. Branzoi, M. Iordoc, F. Branzoi, R. Vasilescu-Mirea, G. Sbarcea, Influence of diamond-like carbon coating on the corrosion resistance of the NITINOL shape memory alloy. *Surf. Interface Anal.* **42**, 502–509 (2010).
72. E. Karshalev, B. Esteban-Fernández de Ávila, J. Wang, Micromotors for "Chemistry-on-the-Fly". *J. Am. Chem. Soc.* **140**, 3810–3820 (2018).
73. 6.Y. Hu, W. Liu, Y. Sun, Multiwavelength phototactic micromotor with controllable swarming motion for "Chemistry-on-the-Fly". *ACS Appl. Mater. Interfaces* **12**, 41495–41505 (2020).
74. Z. Wu, T. Si, W. Gao, X. Lin, J. Wang, Q. He, Superfast near-infrared light-driven polymer multilayer rockets. *Small* **12**, 577–582 (2016).
75. M. Xuan, Z. Wu, J. Shao, L. Dai, T. Si, Q. He, Near infrared light-powered janus mesoporous silica nanoparticle motors. *J. Am. Chem. Soc.* **138**, 6492–6497 (2016).
76. D. Hao, Y. Yang, B. Xu, Z. Cai, Bifunctional fabric with photothermal effect and photocatalysis for highly efficient clean water generation. *ACS Sustain. Chem. Eng.* **6**, 10789–10797 (2018).
77. M. Thommes, K. Kaneko, A. V. Neimark, J. P. Olivier, F. Rodriguez-Reinoso, J. Rouquerol, K. S. W. Sing, Physisorption of gases, with special reference to the evaluation of surface area and pore size distribution (IUPAC Technical Report). *Pure Appl. Chem.* **87**, 1051–1069 (2015).
78. W. Xing, M. Yin, Q. Lv, Y. Hu, C. Liu, J. Zhang, 1 - Oxygen Solubility, Diffusion Coefficient, and Solution Viscosity, in *Rotating Electrode Methods and Oxygen Reduction Electrocatalysts*, W. Xing, G. Yin, J. Zhang, Eds. (Elsevier, 2014), pp. 1–31.
79. J. M. Brown, The hypoxic cell: A target for selective cancer therapy—Eighteenth Bruce F. Cain memorial award lecture. *Cancer Res.* **59**, 5863–5870 (1999).

Acknowledgments: We thank Y. Yu for the help with cell culture and imaging, V. Duppel for SEM imaging, and S. Emmerling for BET measurements. **Funding:** This work is funded by the Max Planck Society, the European Research Council (ERC) Advanced Grant SoMMoR project with grant no. 834531, the ERC Starting Grant COFLeaf project with grant no. 639233, the

Deutsche Forschungsgemeinschaft (DFG) via the cluster of excellence "e-conversion" (project number EXC2089/1–390776260), and by the Center for NanoScience (CENS). **Author contributions:** V.S., F.P., M.S., J.K., and B.V.L. conceived and planned the research. V.S., F.P., Y.A., J.K., L.G., and V.K. performed the experiments or assisted in their realization. All authors contributed to the analysis and discussion of the data. M.S., F.P., and B.V.L. supervised the research. V.S. and F.P. wrote the manuscript with assistance from all other authors. **Competing interests:** The authors declare that they have no competing interests. **Data and materials availability:** All data needed to evaluate the conclusions in the paper are present in the paper or the Supplementary Materials.

Submitted 28 August 2021
Accepted 17 December 2021
Published 19 January 2022
10.1126/scirobotics.abm1421

Science Robotics

Light-driven carbon nitride microswimmers with propulsion in biological and ionic media and responsive on-demand drug delivery

Varun Sridhar, Filip Podjaski, Yunus Alapan, Julia Kröger, Lars Grunenberg, Vimal Kishore, Bettina V. Lotsch, and Metin Sitti

Sci. Robot. **7** (62), eabm1421. DOI: 10.1126/scirobotics.abm1421

Science Robotics (ISSN 2470-9476) is published by the American Association for the Advancement of Science. 1200 New York Avenue NW, Washington, DC 20005. The title *Science Robotics* is a registered trademark of AAAS.